

# A kinematic study of the integral shaped filament: what roles do filaments play in forming young stellar clusters?

Gang Wu<sup>1,2,3</sup>, Esimbek Jarken<sup>1,2</sup>, Willem Baan<sup>4</sup>, Jian-Jun Zhou<sup>1,2</sup>, Dong-Dong Zhou<sup>1,3</sup>, Xiao-Hong Han<sup>1</sup> and Aldiyar Agishev<sup>5</sup>

<sup>1</sup> Xinjiang Astronomical Observatory, Chinese Academy of Sciences, Urumqi 830011, China; [wug@xao.ac.cn](mailto:wug@xao.ac.cn)

<sup>2</sup> Key Laboratory of Radio Astronomy, Chinese Academy of Sciences, Urumqi 830011, China

<sup>3</sup> University of Chinese Academy of Sciences, Beijing 100049, China

<sup>4</sup> Netherlands Institute for Radio Astronomy, NL-7991 PD Dwingeloo, the Netherlands

<sup>5</sup> Faculty of Physics and Technology, Al-Farabi Kazakh National University, Almaty, 050049, Kazakhstan

Received 2017 October 11; accepted 2018 March 31

**Abstract** Young protoclusters (embedded stellar clusters) are responsible for the vast majority of star formation currently occurring in the Galaxy. Recent observations suggest a scenario in which filamentary structures in the interstellar medium represent the first step towards precluster clumps and eventually star formation. Whether filaments continuously fuel the star formation process when the cluster accretes material is still an open question. In this paper, we present a case study of the famous ‘integral shaped filament’ (ISF) in the Orion A molecular cloud and we seek to study the kinematics which is truly originated from the ISF. We firstly define the central ridge of the ISF with  $\text{NH}_3$ ,  $^{12}\text{CO}$ ,  $^{13}\text{CO}$  and  $\text{N}_2\text{H}^+$ . Undulations are present in all the ridges. Moreover, a large scale offset is apparent in the ridges as derived by different tracers, which may be explained by the slingshot mechanism proposed by Stutz & Gould. We fit the velocity field of the ISF and find the derived velocity gradient is about  $0.7 \text{ km s}^{-1} \text{ pc}^{-1}$  which may come from an overall contraction. We propose a method to check the accretion flow along the ISF by using the velocity deviations of different molecular tracers, which is better than the common method of using the velocity distribution of one tracer alone. Using the velocity deviations, we also find that OMC-1 to 5 are located close to the local extrema of the fluctuations, which may demonstrate that gas flows toward each clump along the ISF.

**Key words:** ISM: clouds — ISM: structure — ISM: kinematics and dynamics — stars: formation

## 1 INTRODUCTION

Young protoclusters (embedded stellar clusters) are the locations of the vast majority of current star formation in the Galaxy. As the primary sites of star birth in molecular clouds, protoclusters are a promising laboratory for studying the origin and early evolution of stars and planetary systems (Lada & Lada 2003). One particular issue we need to understand is the origin of the mass supply for the stars that form in these clusters. Is all of the mass already in place before the first stars are born, or is there an extended period during which accreted material continuously fuels the star formation process (Kirk et al. 2013)?

Recent observational studies, especially using the sensitive *Herschel* far infrared data, reveal filamentary structures to be omnipresent in molecular clouds (e.g. André et al. 2010; Stutz & Kainulainen 2015). Moreover, according to a “globular-filament” scenario of star formation (Schneider & Elmegreen 1979; André et al. 2014), filamentary structures in the interstellar medium represent the first step towards precluster clumps (and also prestellar cores) and eventually towards star formation. The densest filaments would then fragment into clumps/cores owing to gravitational instability (Jackson et al. 2010; André et al. 2014). Moreover, according to

sensitive *Herschel* images, most star formation occurs on the filamentary structures (e.g. André et al. 2014). Therefore, it is reasonable to speculate that clump growth occurs primarily through filamentary accretion.

Clump or core growth through filamentary accretion is seen in a number of numerical model simulations, where Balsara et al. (2001) were the first to discuss accretion via filaments and show that their model was consistent with observations of the S106 molecular cloud. Accretion onto dense filaments is also seen in numerical simulations by Gómez & Vázquez-Semadeni (2014). They discuss the velocity field of the filaments and their environment, and how the filaments refocus the accretion of gas toward embedded cores. In observational data, Kirk et al. (2013) revealed the velocity gradients toward the central hub and suggest that material is flowing along the filaments at rates similar to the current local star-formation rate. However, there is still limited observational evidence to clearly show filamentary accretion. That is partly because it is hard to distinguish the contribution of other motions (i.e. rotation) and of star forming processes (e.g. outflow) to the velocity patterns. Moreover, the motions of the diffuse gas around filaments also need to be separated in order to determine the motions of the filaments.

Filament-cluster systems such as the ‘integral shaped filament’ (ISF) in the Orion A cloud present a unique opportunity to gain understanding of cluster formation. The Orion complex is the nearest and probably best studied high-mass star formation region. Orion A is the largest molecular cloud ( $\sim 31.5 \text{ deg}^2$ ) in the Orion complex (Wilson et al. 2005; Stutz & Kainulainen 2015). The ISF is the compact ridge at the northern end of the cometary Orion A cloud (Bally 2008; Johnstone & Bally 1999; Stutz & Gould 2016). At a distance of about 383 pc (Kounkel et al. 2017), it can be observed with good linear resolution even with a radio telescope of modest size. The Orion A cloud is located about 15 degrees below the Galactic plane, leading to a less confused background than typically encountered along the Galactic plane.

In our previous paper (Wu et al. 2017, hereafter Paper I), we have given an overview of ISF using our uniform and fully-sampled  $\text{NH}_3$  maps and discuss the morphology, fragmentation, kinematics and temperature properties in this region. In this study, we focus on the detailed kinematics in the ISF in order to understand whether filamentary structures in the molecular cloud fa-

cilitate clump accretion. This paper is organized as follows.

In Section 2 we describe the observations and database archives. In Section 3 we describe the geometry and velocity distribution of the ISF. In Section 4 we define the central ridge of the ISF, then we carefully fit the velocity gradient by excluding the diffuse gas and discuss the overall accretion flow along the filament. In Section 5 we seek to use the relative motions of different molecular tracers to identify accretion flows along the ISF between the locations of clumps. Finally a summary is presented in Section 6.

## 2 OBSERVATIONS AND DATABASE ARCHIVES

### 2.1 Ammonia - $\text{NH}_3$

The  $\text{NH}_3$  (1, 1) (23.694495 GHz) observations of the ISF presented here were carried out in January 2014 with the 25 m radio telescope, operated by Xinjiang Astronomical Observatory, Chinese Academy of Sciences. This telescope has a beamwidth (full width at half maximum, FWHM) of about  $2'$  (0.22 pc at the distance of 383 pc) and a velocity resolution of  $0.098 \text{ km s}^{-1}$  at 23 GHz provided by an 8192 channel Digital Filter Bank in the 64 MHz bandwidth mode. Spectral fluxes were calibrated against periodically (6 s) injected signals from a noise diode. The pointing and tracking accuracy of the telescope is better than  $18''$ . A 22–24.2 GHz dual polarization channel superheterodyne receiver was used as a frontend with a typical system temperature of about 50 K at 23 GHz on a  $T_{\text{A}}^*$  scale. The maps were made using the on-the-fly (OTF) mode with  $6' \times 6'$  grid size and a  $30''$  sample step under excellent weather conditions and at elevations above  $20^\circ$ .

### 2.2 Carbon Monoxide - CO

The archival  $^{12}\text{CO}$  and  $^{13}\text{CO}$  spectra were observed with the IRAM 30 m telescope at Pico Veleta, Spain, in March, April and October 2008. The data were obtained with the HETERODYNE RECEIVER ARRAY (HERA, nine dual polarization pixels arranged in the form of a  $3 \times 3$  array with  $24''$  spacing) with each polarization tuned to the  $^{12}\text{CO}(2-1)$  line at 230.5 GHz and the  $^{13}\text{CO}(2-1)$  line at 220.4 GHz with a spatial beamwidth of about  $11''$  (0.02 pc at the distance of 383 pc). The main beam efficiencies were 0.524 and 0.545 for  $^{12}\text{CO}(2-1)$  and  $^{13}\text{CO} \text{ m}(2-1)$  respectively. The VERSATILE SPECTROMETRIC AND POLARIMETRIC ARRAY (VESPA) backend provided a

spectral resolution of 320 kHz (i.e.  $0.4 \text{ km s}^{-1}$ ). The maps were made using the OTF mode with  $5''$  data sampling in right ascension, and with steps of  $12''$  in declination (see Berné et al. 2014, for more details).

### 2.3 Diazenylium - $\text{N}_2\text{H}^+$

The archival observations of  $\text{N}_2\text{H}^+$  (1–0) at 93.1737767 GHz were carried out using the 45 m radio telescope of Nobeyama Radio Observatory from 2005 May 11 to 20, and from 2007 March 4 to 9. The employed receiver frontend was the 25-element focal-plane SIS array receiver BEARS. The half-power beamwidth for the element beam of BEARS was  $17.8'' \pm 0.4''$  (0.03 pc at a distance of 383 pc) and the spectral resolution was 37.8 kHz (corresponding to  $0.12 \text{ km s}^{-1}$ ) at 93 GHz (for more details see Tatematsu et al. 2008).

## 3 THE GEOMETRY AND VELOCITY FIELD OF THE ISF

The  $\text{NH}_3$  (1, 1) velocity-integrated line intensity (zeroth moment) map is presented as gradations of grey scale intensities and contours in the left panel of Figure 1. The integration range is from  $6.5$  to  $12.5 \text{ km s}^{-1}$  to cover the main line of  $\text{NH}_3$  (1, 1). Contours start at  $0.18 \text{ K km s}^{-1}$  ( $4\sigma$ , thick grey line) and go up in steps of  $0.18 \text{ K km s}^{-1}$  (thin grey lines).  $\sigma$  equals  $\text{rms} \times \Delta V \times \sqrt{N_{\text{channels}}}$ , where ‘rms’ is the averaged baseline channel root mean square exported from the baseline fitting with CLASS from the GILDAS package of all spectra,  $\Delta V$  is the channel spacing and  $N_{\text{channels}}$  is the channel number in the integrated velocity range ( $6.5$  to  $12.5 \text{ km s}^{-1}$ ). The limits of the mapped region are indicated with green dashed lines. The red line in the top right of the left panel illustrates the 1 pc scale at a distance of 383 pc (Kounkel et al. 2017). The whole map consists of a total of 45 240 raw spectra, covering a region about  $1.2^\circ$  in declination and about  $0.6^\circ$  in right ascension. The right panel of Figure 1 displays intensity-weighted velocity (first moment, color image) overlaid with  $\text{NH}_3$  (1, 1) integrated intensity contours as in the left panel in Figure 1. A clear velocity gradient can be seen along the main part of the ISF from the first moment image. This velocity gradient will be used for model fitting in Section 4.

In each panel of Figure 1, the Trapezium cluster has been labeled as a blue star and the half-power beam is illustrated as a black filled circle at the bottom right. The known clumps OMC-1 to 5 (Johnstone & Bally 1999,

2006) are labeled in the left panel. The zeroth moment map of  $\text{NH}_3$  (1, 1) shows an integral shaped morphology ( $\int$ ) as firstly observed in  $^{13}\text{CO}$  (see Bally et al. 1987). The  $^{12}\text{CO}$  and  $^{13}\text{CO}$  zeroth moment maps have been presented in figure 2 and figure 3 respectively of Berné et al. (2014) and the  $\text{N}_2\text{H}^+$  zeroth moment map in figure 1 of Tatematsu et al. (2008). These observations all display similar morphologies as  $\text{NH}_3$  (1, 1).

## 4 THE VELOCITY GRADIENT ALONG THE ISF

### 4.1 The Central Ridge of ISF

In the following sections, the velocity structure along the central ridge of the ISF will be investigated. In order to determine the location of this central ridge, we follow the strategy in Kirk et al. (2013) by first selecting only spectral features with an integrated intensity that is 5 times that expected from the noise level (the spectral rms times the square root of the number of velocity channels). In addition, these must have a minimum of two adjacent spectral channels also showing emission larger than 5 times their spectral rms. Next we search for the location of the peak in velocity-integrated line intensity along every horizontal cut through the filament. Finally, we exclude several points which are away from the main filament structure (seven points in  $^{12}\text{CO}$ , six points in  $\text{NH}_3$  and five points in  $^{13}\text{CO}$ ).

The derived locations of the  $\text{NH}_3$  ridge (red polyline), the  $^{12}\text{CO}$  ridge (green polyline), the  $^{13}\text{CO}$  ridge (cyan polyline) and the  $\text{N}_2\text{H}^+$  ridge (yellow polyline) are all presented in Figure 2. Firstly as we can see in the figure, these ridges derived with different tracers are in close proximity but they also show some differences. A significant feature is that undulations are present in all the ridges. Moreover, a large scale offset is present in the ridges derived by different tracers, i.e. in OMC-3 the  $\text{N}_2\text{H}^+$  ridge (yellow) and  $\text{NH}_3$  ridge (red) are significantly displaced from the CO ridges (green and cyan). Stutz & Gould (2016) noticed that there are undulations in the gas column ridge (and also velocity) and proposed a slingshot mechanism in which the undulations appear to be ejecting protostars. Although it is not directly proved from Figure 2, these undulations and offset may come from the oscillating filament associated with an ejecting protostar and protocluster in the slingshot mechanism scenario (Stutz & Gould 2016; Stutz 2018).

As  $\text{NH}_3$  could be enhanced by the hot dense gas (Wiseman & Ho 1998), it would be less contaminated

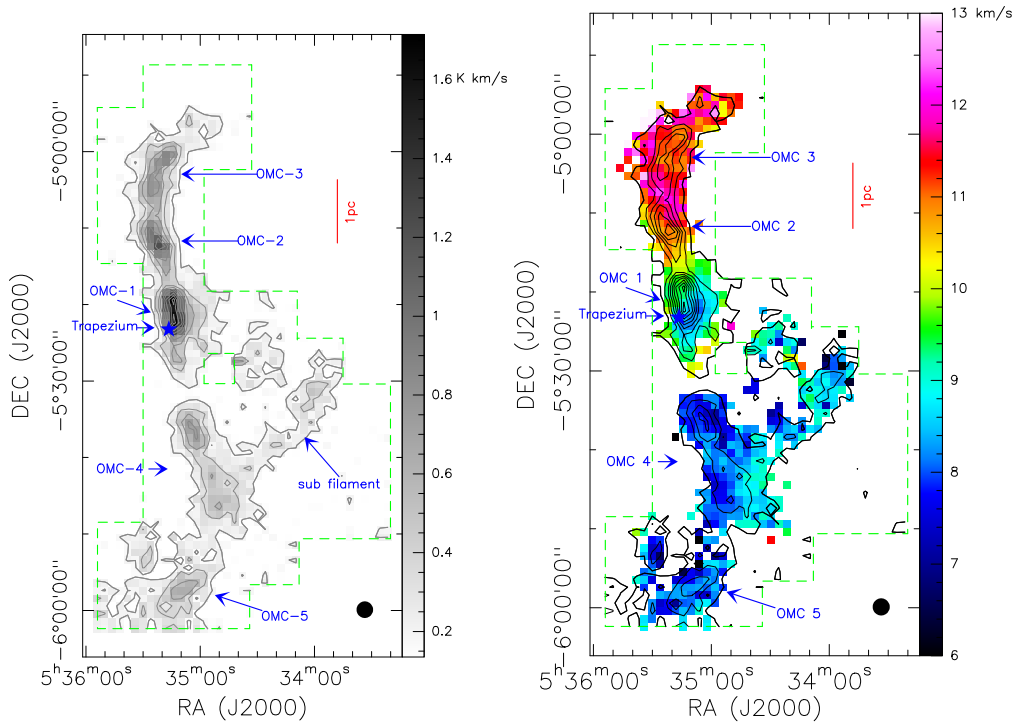


**Fig. 1** *Left*: Integrated intensity (zeroth moment) map of  $\text{NH}_3$  (1, 1). The integration range of each panel is  $6.5 < V_{\text{LSR}} < 12.5 \text{ km s}^{-1}$ . Contours start at  $0.18 \text{ K km s}^{-1}$  ( $4\sigma$ ) and go up in steps of  $0.18 \text{ K km s}^{-1}$ . The limits of the mapped region are indicated with *green dashed lines*. A *blue star* in each panel indicates the Trapezium cluster and *black filled circles* in the lower right illustrate the half-power beam size. *Right*: Intensity-weighted (first moment) velocity map (color image) of the ISF. Superposed contours are the same as those in the left panel.

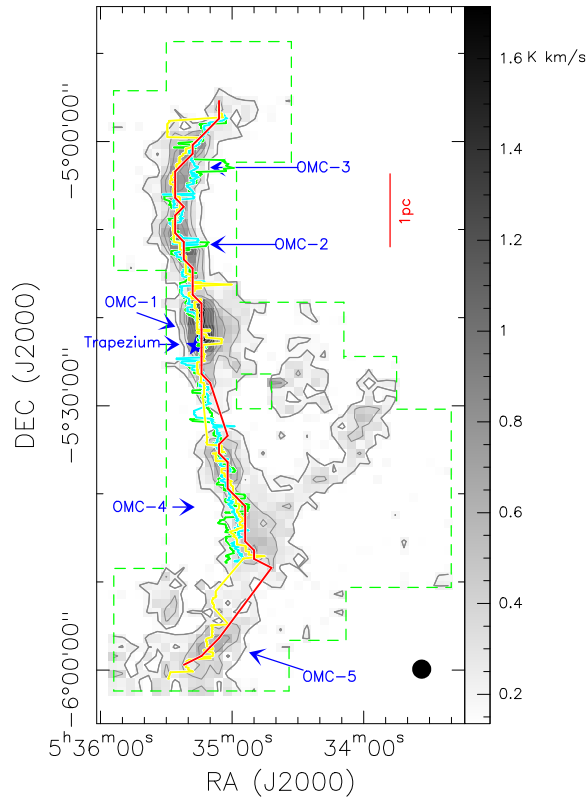


**Fig. 2** Central ridges derived from  $\text{NH}_3$  (red),  $^{12}\text{CO}$  (green),  $^{13}\text{CO}$  (cyan) and  $\text{N}_2\text{H}^+$  (yellow). Contours are the same as those in Fig. 1 (*left panel*).

by the diffuse gas. In the following section, we adopt the  $\text{NH}_3$  ridge as a unifying ridge for the ISF.

## 4.2 The Velocity Gradient Fitting

In order to quantitatively investigate the clear velocity gradient running along the main part of the ISF (see Section 3), we seek to fit this velocity gradient by the following steps:

- (1) After excluding the spectral data with poor signal to noise ratio (S/N) as described in Section 4.1, we also exclude the diffuse components around the ISF by only considering data within  $4'$  (or a radius of 0.45 pc at 383 pc) of the central ridge determined with  $\text{NH}_3$ .
- (2) We fit  $\text{NH}_3$  (1, 1) spectra using the GILDAS<sup>1</sup> built-in ‘ $\text{NH}_3$  (1, 1)’ fitting method, which can fit all 18 components simultaneously. The  $^{12}\text{CO}$  and  $^{13}\text{CO}$  spectra are fitted using a single-component GILDAS built-in ‘GAUSS’ fitting method. Similarly, the  $\text{N}_2\text{H}^+$   $J = 1 - 0$ ,  $F = 2 - 1$  spectra are fitted using the GILDAS built-in ‘HFS’ fitting method, which can fit all seven components simultaneously with their theoretical intensity ratios and frequency separations.
- (3) The velocity gradient along the ISF is fitted following the procedure outlined in Goodman et al. (1993) assuming a simple linear form for the centroid velocities:  $V_{\text{LSR}} = v_0 + a \times \delta\alpha + b \times \delta\beta$ , where  $\delta\alpha$  and  $\delta\beta$  are offsets in right ascension and declination respectively (in radians), and  $v_0$  represents the systemic velocity of the cloud. Then the velocity gradient is given by  $\nabla v = (a^2 + b^2)^{0.5}/D$  at a distance of  $D$  and the direction of increasing velocity by  $\theta = \tan^{-1}(a/b)$ .

To fit the velocity gradient, the Python routine LMFT (Newville et al. 2016) is used to find the best-fitting values to the constants  $a$ ,  $b$  and  $v_0$ , and then to convert the angular velocity gradients to a physical scale assuming a distance of 383 pc. The derived  $\nabla v$  and  $\theta$  of  $\text{NH}_3$  are  $0.57 \text{ km s}^{-1} \text{ pc}^{-1}$  and  $28.0^\circ$  respectively. An image of the fitting velocities in the pixels with  $\text{S/N} > 5$  is presented in Figure 3, which accurately recovers the observed velocity gradient in Figure 1. Similarly, we also fit the velocity gradients with the  $^{12}\text{CO}$ ,  $^{13}\text{CO}$  and  $\text{N}_2\text{H}^+$  data. For  $^{12}\text{CO}$ ,  $\nabla v$  and  $\theta$  are  $0.55 \text{ km s}^{-1} \text{ pc}^{-1}$  and  $14.2^\circ$  respectively. For  $^{13}\text{CO}$ ,  $\nabla v$  and  $\theta$  are  $0.58 \text{ km s}^{-1} \text{ pc}^{-1}$  and  $15.9^\circ$  respectively. For

$\text{N}_2\text{H}^+$ ,  $\nabla v$  and  $\theta$  are  $1.09 \text{ km s}^{-1} \text{ pc}^{-1}$  and  $60.5^\circ$  respectively. The direction and magnitude of the fitted gradients towards the north are only slightly different for all molecules except for  $\text{N}_2\text{H}^+$ . We suspect this exception for  $\text{N}_2\text{H}^+$  comes from the poor S/N of the  $\text{N}_2\text{H}^+$ .

Using the well defined ridges, we fit the velocity gradient based on gas near the ISF ridges (within  $4'$ ) which largely excludes gas which may not be part of the ISF. The derived velocity gradient is associated with the previous study (e.g. Bally et al. 1987). This indicates that the diffuse gas and the main part of the ISF are a co-rotating structure. We assume an inclination of  $60^\circ$  with respect to the line of sight, which is a median inclination of randomly oriented filaments (e.g. Hanawa et al. 1993). In the following, we adopt a de-projected velocity gradient of  $0.57 / \sin(60^\circ) \sim 0.7 \text{ km s}^{-1} \text{ pc}^{-1}$ .

## 4.3 Is there Accretion Flow along the Filament?

The origin of the velocity gradient in the ISF is still an open question. Kutner et al. (1977) and Wilson et al. (2005) argued this velocity gradient results from an overall rotation. Hacar et al. (2017) stated this velocity gradient is from an overall accretion flow toward OMC-1. If the gradient is interpreted as rotation, we take the ISF as a homogeneous rigidly rotating cylinder, and the ratio of rotational to gravitational energy is

$$\begin{aligned} \beta &= \frac{E_{\text{rot}}}{E_{\text{grav}}} \\ &= \frac{1}{2} \frac{ML^2}{12} \left(1 + \frac{3}{2x^2}\right) \omega^2 / \frac{3}{2} \frac{GM^2}{L} f(x) \quad (1) \\ &\approx \frac{\omega^2}{4\pi G\rho} \frac{L^2}{9R^2}, \end{aligned}$$

where  $G$  is the gravitational constant and  $\rho$ ,  $L$ ,  $R$  and  $\omega$  are the constant density, height, radius and angular velocity of the cylinder respectively.  $x \equiv L/D$  and  $f(x) \sim 1$  (Bonnell et al. 1992). We can also write it as

$$\beta = \frac{3.0 \times 10^{-3} \omega_{-14}^2}{n_4} \frac{L^2}{9R^2}, \quad (2)$$

where  $\omega_{-14}$  is the angular velocity in units of  $10^{-14} \text{ s}^{-1}$  and  $n_4$  is the gas density in units of  $10^4 \text{ cm}^{-3}$  (Menten et al. 1984; Levshakov et al. 2013). The length of the ISF is about 7 pc (see Fig. 1), and the width is about 1 pc at a distance of 383 pc. Assuming an angular velocity of  $2.1 \times 10^{-14} \text{ s}^{-1}$  (corresponding to the velocity gradient of  $0.7 \text{ km s}^{-1} \text{ pc}^{-1}$ ) and an average density of  $10^4 \text{ cm}^{-3}$  (Johnstone & Bally 1999) for the ISF, then  $\beta \sim 0.1$ .

<sup>1</sup> <http://www.iram.fr/IRAMFR/GILDAS/>

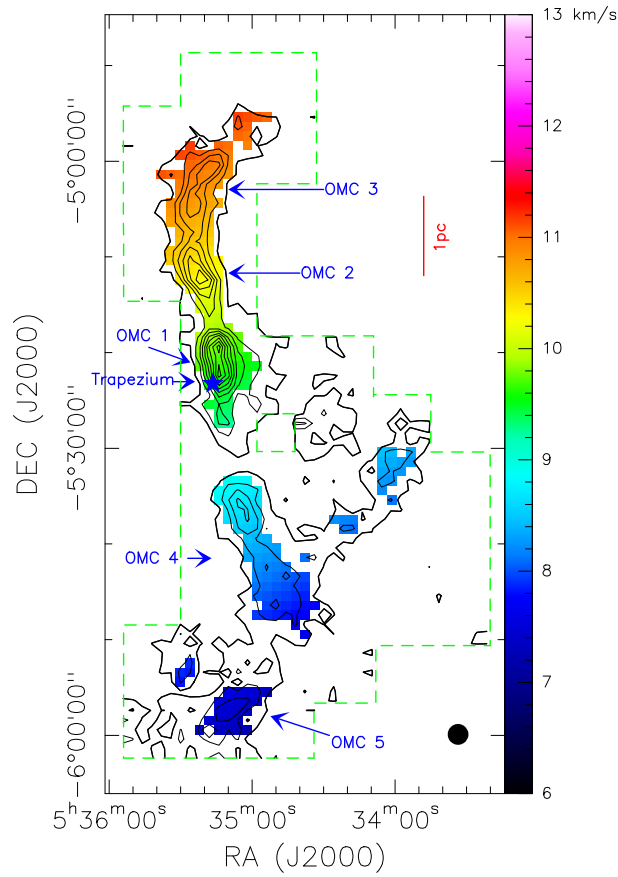


**Fig. 3** The image of the fitted velocities generated by the model of the ISF. Contours are the same as those in Fig. 1 (*left panel*).

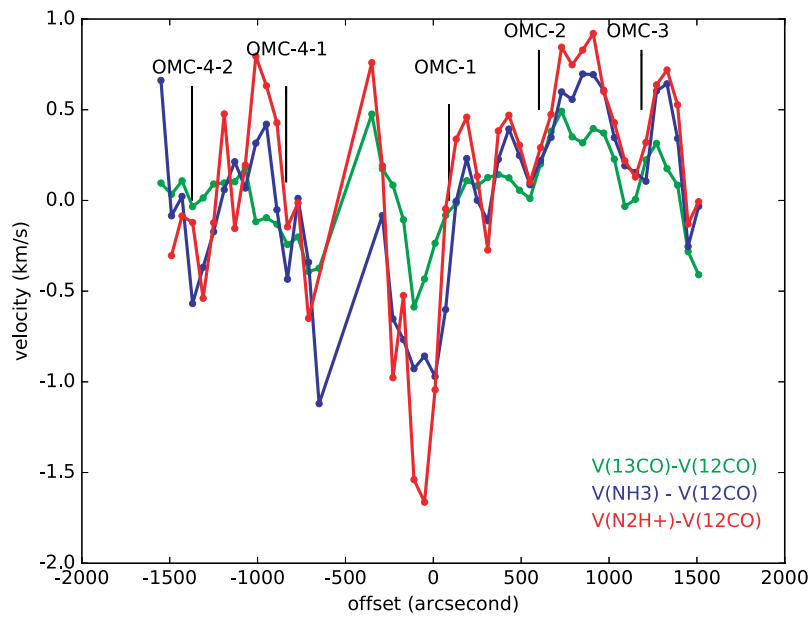


**Fig. 4** The centroid velocity deviations between  $^{13}\text{CO}$  and  $^{12}\text{CO}$  (*green*),  $\text{NH}_3$  and  $^{12}\text{CO}$  (*blue*), and  $\text{N}_2\text{H}^+$  and  $^{12}\text{CO}$  (*red*).

Thus, the rotational energy is a small fraction of the gravitational energy. For an isothermal filament, the free fall time in the filament is  $t_{\text{ff}} = \frac{1}{2}(G\rho)^{-1/2} \sim 0.3 \text{ Myr}$  (Tan et al. 2014), which is much less than the estimated age of the ISF (i.e. 10 Myr as suggested by Carpenter (2000)). Therefore, even if the ISF was initially rotating, infall motions would rapidly dominate over rotation.

If the velocity gradient results from contraction from opposite ends of the filament instead of rotation, we can estimate the accretion rate onto the center region of OMC-1 as

$$\dot{M}_{\parallel} = \frac{\nabla V_{\parallel} M}{\tan(\alpha)}, \quad (3)$$

where  $\nabla V_{\parallel}$  is the velocity gradient observed along the line of sight,  $M$  is the mass of the ISF and  $\alpha$  is the inclination of the ISF (Kirk et al. 2013). We can also write this as

$$\dot{M}_{\parallel} = \frac{\nabla V_{\parallel} n_e * \pi R^2 L}{\tan(\alpha)}. \quad (4)$$

If the accretion flow leads into the central OMC-1, the accretion rate along the ISF is  $3.71 M_{\odot} \text{ Myr}^{-1}$ . In all the discussions above, with the well defined velocity gradient and ridge, we could interpret the velocity gradient along the ISF to be contraction.

## 5 RELATIVE MOTIONS OF DIFFERENT MOLECULAR TRACERS

Filamentary structures of molecular clouds are proposed as accretion channels for their own clumps, which are believed to lead to a see-saw velocity distribution along the filament (e.g. Zhang et al. 2015). However, as discussed in Paper I, a see-saw velocity distribution could also result from feedback of the clusters (cores) in the filament or the nearby HII region, and not necessarily from the accretion flow.

In this work, we propose a new method to identify accretion flows along the ISF relative to the location of clumps by using the velocity differences between molecular tracers with different optical depths. For this purpose, spectra are sequenced within  $1'$  from the filament's  $\text{NH}_3$  peak ridge and any spectra with poor S/N are excluded. At each location along the ISF ridge, the velocity differences between the spectra of  $^{13}\text{CO}$  and  $^{12}\text{CO}$ , those of  $\text{NH}_3$  and  $^{12}\text{CO}$ , and those of  $\text{N}_2\text{H}^+$  and  $^{12}\text{CO}$  are presented in Figure 4 as green, blue, and red lines, respectively. The locations of the clumps OMC-1, OMC-2, OMC-3, OMC-4-1 and OMC-4-2 are also labeled in Figure 4. It is clear that all the clumps are found near the

local extrema in the velocity difference fluctuations. The fact that all clumps are found near local extrema could be explained by the accretion flow to each protocluster as suggested by, e.g., Hacar & Tafalla (2011) and Zhang et al. (2015). However, as proposed by Stutz (2018), clusters may also be formed by the slingshot mechanism. This velocity distribution could also be explained by an oscillating filament. Moreover, Stutz & Gould (2016) already showed that the  $^{13}\text{CO}$  gas velocity ridgeline is offset significantly from the  $\text{N}_2\text{H}^+$  ridge (see their fig. 9).

However, optical depth effects may potentially play a role in this difference. Since the hyperfine fit to the  $\text{NH}_3$  and  $\text{N}_2\text{H}^+$  corrects for optical depth broadening, no correction is applied to the CO data. Moreover, we should note that, unlike a quiescent filament, e.g. L1517, the ISF is an active star formation region. There are lots of protostars embedded in the filament (e.g. Stutz et al. 2013). The velocity deviations and also the undulations in the ridges of the ISF (see Section 4.1) may come from feedback of the protostars.

## 6 SUMMARY

Using the spectra of  $^{12}\text{CO}$ ,  $^{13}\text{CO}$ ,  $\text{NH}_3$  and  $\text{N}_2\text{H}^+$  in the ISF, we study kinematic structure in the ISF to seek a clearer understanding of whether filamentary structures in the molecular cloud facilitate accretion. We find the ISF is likely to facilitate accretion along the main axis of the filament. The main conclusions of this work are as follows:

- (1) We determine the location of the ridges with  $\text{NH}_3$ ,  $^{12}\text{CO}$ ,  $^{13}\text{CO}$  and  $\text{N}_2\text{H}^+$  tracers and find these ridges are close to each other, but there are also some differences. Undulations are present in all the ridges. Moreover, a large scale offset is present in the ridges derived by different tracers which may come from the slingshot mechanism proposed by Stutz & Gould (2016).
- (2) We derive a de-projected velocity gradient along the ISF of about  $0.7 \text{ km s}^{-1} \text{ pc}^{-1}$  and find that the associated rotational energy is only about 10% of the gravitational energy. Therefore, the velocity gradient may signify an accretion flow along the filament. If all the accretion flow leads into the central OMC-1, the accretion rate would be  $3.71 M_{\odot} \text{ Myr}^{-1}$ .
- (3) In order to identify any accretion flow along the ISF into the clumps, we employed a new method using the velocity differences of molecular tracers. The

clumps are all found to be located near the local extrema of the velocity differences. This could be explained by the accretion flow to each protocluster. However, this could also be explained by the sling-shot mechanism (Stutz 2018).

**Acknowledgements** This work was funded by the CAS “Light of West China” Program (2015-XBQN-B-03), the National Natural Science Foundation of China (Grant Nos. 11433008 and 11603063), partly supported by the National Natural Science Foundation of China (Grant Nos. 11703073, 117030734, 11373062 and 11303081) and Recruitment Program of High-end Foreign Experts (20166500004).

## References

- André, P., Di Francesco, J., Ward-Thompson, D., et al. 2014, *Protostars and Planets VI*, 27
- André, P., Men’shchikov, A., Bontemps, S., et al. 2010, *A&A*, 518, L102
- Bally, J. 2008, Overview of the Orion Complex, ed. B. Reipurth, *Handbook of Star Forming Regions (The Northern Sky ASP Monograph Publications)*, 459
- Bally, J., Langer, W. D., Stark, A. A., & Wilson, R. W. 1987, *ApJ*, 312, L45
- Balsara, D., Ward-Thompson, D., & Crutcher, R. M. 2001, *MNRAS*, 327, 715
- Berné, O., Marcelino, N., & Cernicharo, J. 2014, *ApJ*, 795, 13
- Bonnell, I., Arcoragi, J.-P., Martel, H., & Bastien, P. 1992, *ApJ*, 400, 579
- Carpenter, J. M. 2000, *AJ*, 120, 3139
- Gómez, G. C., & Vázquez-Semadeni, E. 2014, *ApJ*, 791, 124
- Goodman, A. A., Benson, P. J., Fuller, G. A., & Myers, P. C. 1993, *ApJ*, 406, 528
- Hacar, A., Alves, J., Tafalla, M., & Goicoechea, J. R. 2017, *A&A*, 602, L2
- Hacar, A., & Tafalla, M. 2011, *A&A*, 533, A34
- Hanawa, T., Nakamura, F., Matsumoto, T., et al. 1993, *ApJ*, 404, L83
- Jackson, J. M., Finn, S. C., Chambers, E. T., Rathborne, J. M., & Simon, R. 2010, *ApJ*, 719, L185
- Johnstone, D., & Bally, J. 1999, *ApJ*, 510, L49
- Johnstone, D., & Bally, J. 2006, *ApJ*, 653, 383
- Kirk, H., Myers, P. C., Bourke, T. L., et al. 2013, *ApJ*, 766, 115
- Kounkel, M., Hartmann, L., Loinard, L., et al. 2017, *ApJ*, 834, 142
- Kutner, M. L., Tucker, K. D., Chin, G., & Thaddeus, P. 1977, *ApJ*, 215, 521
- Lada, C. J., & Lada, E. A. 2003, *ARA&A*, 41, 57
- Levshakov, S. A., Henkel, C., Reimers, D., et al. 2013, *A&A*, 553, A58
- Menten, K. M., Walmsley, C. M., Kruegel, E., & Ungerechts, H. 1984, *A&A*, 137, 108
- Newville, M., Stensitzki, T., Allen, D. B., et al. 2016, *Lmfit: Non-Linear Least-Square Minimization and Curve-Fitting for Python*, *Astrophysics Source Code Library*, ascl:1606.014
- Schneider, S., & Elmegreen, B. G. 1979, *ApJS*, 41, 87
- Stutz, A. M., Tobin, J. J., Stanke, T., et al. 2013, *ApJ*, 767, 36
- Stutz, A. M., & Kainulainen, J. 2015, *A&A*, 577, L6
- Stutz, A. M., & Gould, A. 2016, *A&A*, 590, A2
- Stutz, A. M. 2018, *MNRAS*, 473, 4890
- Tan, J. C., Beltrán, M. T., Caselli, P., et al. 2014, *Protostars and Planets VI*, 149
- Tatematsu, K., Kandori, R., Umemoto, T., & Sekimoto, Y. 2008, *PASJ*, 60, 407
- Wilson, B. A., Dame, T. M., Mashedier, M. R. W., & Thaddeus, P. 2005, *A&A*, 430, 523
- Wiseman, J. J., & Ho, P. T. P. 1998, *ApJ*, 502, 676
- Wu, Gang, Qiu, Keping, Esimbek, Jarken, et al. 2017, *A&A*, submitted
- Zhang, Q., Wang, K., Lu, X., & Jiménez-Serra, I. 2015, *ApJ*, 804, 141